Journal of ELECTRONIC MATERIALS
DOI: 10.1007/s11664-014-3029-1
© 2014 TMS

# GaSb Thermophotovoltaic Cells Grown on GaAs Substrate Using the Interfacial Misfit Array Method

DANTE DEMEO,[1] COREY SHEMELYA,[1] CHANDLER DOWNS,[1] ABIGAIL LICHT,[1] EMIR SALIH MAGDEN,[1] TOM ROTTER,[2] CHETAN DHITAL,[3] STEPHEN WILSON,[3] GANESH BALAKRISHNAN,[2] and THOMAS E. VANDERVELDE[1,4]

1.—Renewable Energy and Applied Photonics Labs, ECE Department, Tufts University, Medford, MA 02155, USA. 2.—Center for High Tech Materials, University of New Mexico, Albuquerque, NM 87131, USA. 3.—Department of Physics, Boston College, 140 Commonwealth Avenue, Chestnut Hill, MA 02467, USA. 4.—e-mail: tvanderv@ece.tufts.edu

We present gallium antimonide (GaSb) *p*–i–*n* photodiodes for use as thermophotovoltaic (TPV) cells grown on gallium arsenide (100) substrates using the interfacial misfit array method. Devices were grown using molecular beam epitaxy and fabricated using standard microfabrication processes. X-ray diffraction was used to measure the strain, and current–voltage (*I*–*V*) tests were performed to determine the photovoltaic properties of the TPV cells. Energy generation at low efficiencies was achieved, and device performance was critically analyzed.

**Key words:** Thermophotovoltaic, interfacial misfit array, lattice mismatch, gallium antimonide

## INTRODUCTION

Thermophotovoltaic (TPV) generation of electricity has shown promise for harvesting energy from many different thermal sources including solar, radioisotope, and waste heat.[1–4] These devices operate using the photovoltaic effect and often employ spectral control such as filters and thermal emitters to better match the spectrum incident on the photodiode,[5] which leads to increased efficiencies. One downside of these devices, however, is the cost of the present material of choice, gallium antimonide (GaSb).

The ability to grow a GaSb TPV cell on a highly lattice-mismatched (LMM) substrate, such as gallium arsenide (GaAs), would reduce the cost of such devices. At the time of writing, GaAs substrates are cheaper by almost a factor of 10 than GaSb, based on online retail prices. Furthermore, GaAs growth on silicon is becoming more common,[6] enabling an even greater reduction in cost. Si substrates are cheaper by a factor of 10 than GaAs, resulting in cost savings of 100× in substrate cost compared with GaSb. This is especially important because TPVs are area dependent; i.e., larger devices are needed in order to generate more power. As such, reducing the cost of thermophotovoltaic diodes is critical to their adoption as an energy harvesting technology. For this reason we examined a GaSb *p*–i–*n* diode grown epitaxially on a GaAs substrate implementing a strain-reducing interfacial misfit (IMF) array layer.

The IMF array is a strain-mitigation technique used to enable epitaxial growth of highly lattice-mismatched materials.[7–10] It is an intentional periodic array of 90° edge dislocations at a heterojunction interface. This is accomplished by engineering the interface through careful control of crystal growth conditions to produce a ratio of atoms equal to the least common multiple of their corresponding lattice constants. IMF is one technique in a cadre of new approaches to improve infrared photodiodes.[11–19] In this work, the interface was GaSb grown epitaxially on a GaAs substrate. Thus, for GaSb and GaAs, with lattice constants of 6.09593 Å and 5.65330 Å, respectively,[20] a ratio of 13:14 will yield a linear distance of approximately 79.15 Å

(Received July 31, 2013; accepted January 9, 2014)

Published online: 04 February 2014

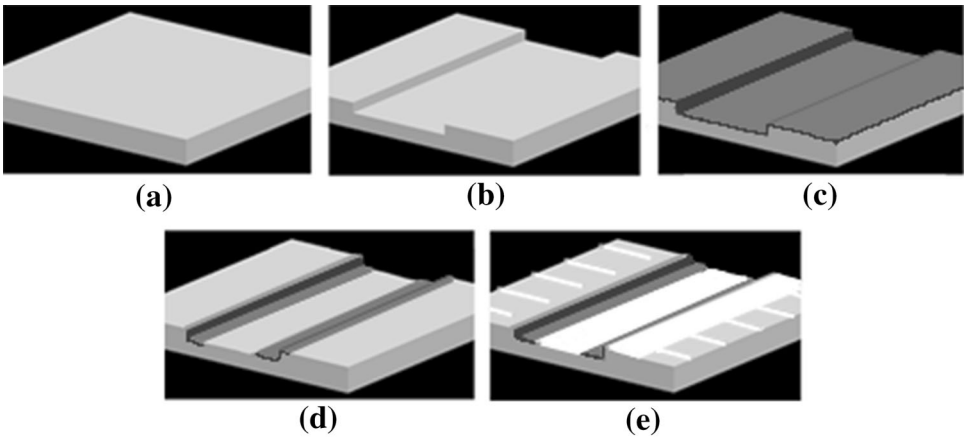


Fig. 1. Overview of photodiode microfabrication process: (a) sample as grown, (b) etch to the bottom contact, (c) coating with $Si_3N_4$, shown in a darker grey, (d) etch of $Si_3N_4$ to create sidewall passivation, (e) metal contacts, shown in white, deposited to connect to a circuit and complete the structure.

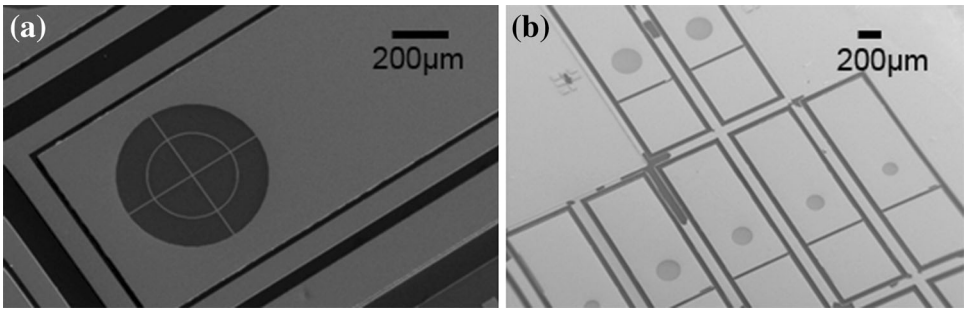


Fig. 2. SEM images of (a) 500-$\mu$m-diameter aperture with contact grid, (b) set of 10 diodes with aperture ranging from 30 $\mu$m to 300 $\mu$m.

{13× [lattice constant of GaSb (110)] = 14 × [lattice constant of GaAs (110)]}. Therefore, to create the IMF array, the two dimensional (2D) packed Sb atoms skip every 14th Ga atom on the GaAs surface, thus establishing the 13:14 ratio. This technique has been investigated on photon-emitting materials before.[7,21–23] However, very little research has been performed for photon-absorption applications,[24] which typically require much higher crystal quality.

This article reports on molecular beam epitaxy (MBE) growth of $p$–i–$n$ photodiodes for TPV energy harvesting. The crystals were grown at the Center for High Technology Materials at the University of New Mexico, processed at the Center for Nanoscale Systems at Harvard University, and tested at Tufts University.

## DEVICE FABRICATION AND EXPERIMENTAL PROCEDURES

The samples were grown on a V-80 solid-source MBE system equipped with As and Sb valved crackers set to yield $As_2$ and Sb, respectively. The device structure consisted of a GaAs substrate, IMF array, 400-nm $n^+$-GaSb back-side field/contact layer, 3500-nm $n$-GaSb, 1500-nm i-GaSb layer, 200-nm $p$-GaSb layer, 50-nm $p^+$-GaSb buffer, a 50-nm $p^+$-AlGaSb window layer, and 10-nm $p^+$-GaSb antioxidation/contact layer. A control sample was made on a GaSb substrate; this sample had the same exact structure with the exception of the IMF layer and substrate material. To create devices from these semiconductor diodes, electrical contacts must be added. The procedure for creating electrical contacts to the bottom contact layer, located just above the IMF layer, and the top contact layer, the 10-nm-thick topmost layer, is described presently.

Diodes were processed using an all-front-side contact pattern. Processing commenced after the sample had been grown according to the above considerations, as depicted in Fig. 1a. The first processing step consisted of a dry etch to the bottom contact in an inductively coupled plasma reactive-ion etcher using a $BCl_3$/Ar chemistry, as shown in Fig. 1b. This was followed by plasma-enhanced chemical vapor deposition (PECVD) of $Si_3N_4$ for passivation and isolation, as shown in Fig. 1c. Another dry etch was used to selectively remove this layer in a capacitively coupled plasma reactive-ion etcher using a $SF_6/O_2$ chemistry, as depicted in Fig. 1d. Finally, Ti-Pt-Au ohmic contacts were deposited via electron beam evaporation and then

lifted off, as shown in Fig. 1e. In this method electrical connections are made to both the top and bottom contact layers of the device.

Two sets of diodes were fabricated: a 500-$\mu$m-diameter pattern, and a set of 10 diodes with different sized apertures with diameter of 30 $\mu$m to 300 $\mu$m in 30 $\mu$m increments. These patterns are shown in Fig. 2. The different patterns followed the same processing procedure but were made using different mask patterns and at different locations on the sample; as such, some variation in performance is to be expected. The darker circular regions shown in Fig. 2 are the apertures of the diode; the apertures define the area of the diode able to be exposed to light. The brighter rectangles around the apertures are the top contacts, and the smaller rectangles directly adjacent are the bottom contacts.

X-ray diffraction measurements were performed with a Bruker D2 Phaser powder diffractometer (Bruker Corp., Billerica, MA). Current–voltage ($I$–$V$) curves were obtained using an Oriel solar simulator (Newport Corp., Irvine, CA) at 9× suns with an AM1.5 filter and probe station. The spectral response was measured using a 1/8-m monochromator, halogen light source, and germanium detector. The light was approximately collimated from the monochromator, and the optical power incident on the diode was measured using a S122C photodiode power sensor (ThorLabs Inc., Newton, NJ). After measuring the incident power on the diode for each wavelength, the light source was focused onto the TPV diode and the electrical output was measured at each wavelength using a Keithley 2400 source meter (Keithley Instruments Inc., Cleveland, OH).

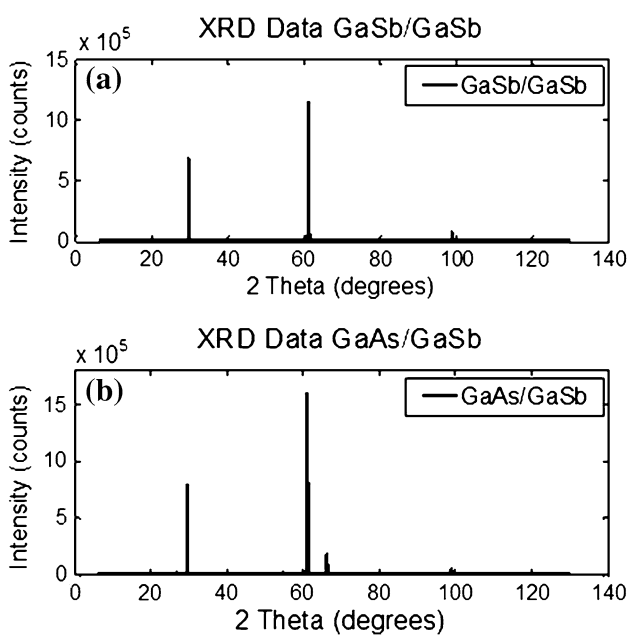


Fig. 3. XRD data for (a) GaSb/GaSb control and (b) GaAs/GaSb IMF sample.

## RESULTS AND DISCUSSION

The strain of the sample was measured by comparing the lattice constants of the IMF grown cell with an epitaxial layer of GaSb on a GaSb substrate. The average lattice constant for both samples was measured from x-ray diffraction (XRD) data and was identical to within 0.001 Å, suggesting that the strain of the GaAs/GaSb material system was compensated. The XRD data are presented in Fig. 3 and Table I.

Figure 4 shows an experimental demonstration of the current–voltage curves for a 500-$\mu$m-diameter IMF diode and control sample. This is a significant demonstration of power generation in an IMF-based GaAs/GaSb strain-compensated diode absorber. However, as in most initial demonstrations, the IMF device exhibits relatively poor diode performance; For example, this IMF absorber has an open-circuit voltage ($V_{OC}$) of 0.094 V, a short-circuit current ($I_{SC}$) of 0.32 mA, and a fill factor (FF) of 25%. These are lower than the control diode, which has a $V_{OC}$ of 0.24 V, $I_{SC}$ of 0.48 mA, and FF of 54%. We believe that these low performance metrics are caused by both parasitic series and shunt resistances, $R_{series}$ and $R_{shunt}$, respectively. The former is evident from the $I$–$V$ curve's deviation from a near-vertical line in region 1 of Fig. 4, between the maximum-power point and open-circuit voltage. The series resistance is most

**Table I. XRD data for GaSb/GaSb control and GaAs/GaSb sample**

| Sample | Material (Order of Interference) | Peak Angle, 2$\theta$ (°) | Lattice Constant (Å) | Average Lattice Constant (Å) |
|---|---|---|---|---|
| GaSb/GaSb control | GaSb ($n$ = 1) | 29.71 | 6.0143 | 6.0561 ± 0.0379 |
| | GaSb ($n$ = 2) | 61.11 | 6.0656 | |
| | GaSb ($n$ = 3) | 98.88 | 6.0883 | |
| GaAs/GaSb sample | GaSb ($n$ = 1) | 29.60 | 6.0361 | 6.0558 ± 0.0278 |
| | GaSb ($n$ = 2) | 61.00 | 6.0754 | |
| | GaAs ($n$ = 3) | 66.33 | 5.6370 | 5.6370 |

The average lattice constant for GaSb for both samples was identical to within 0.001 Å, indicating strain relief in the GaAs/GaSb growth.

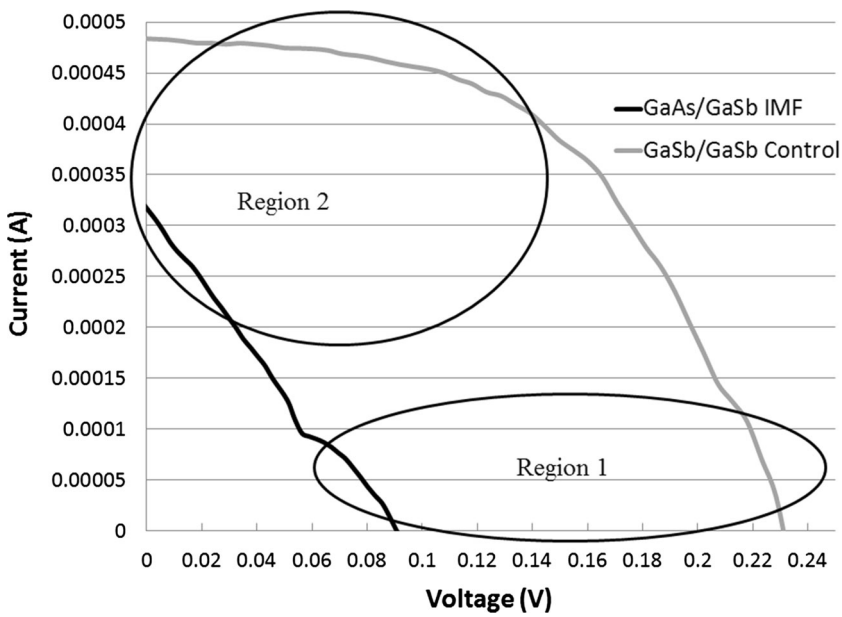


Fig. 4. *I–V* curves for 500-$\mu$m GaAs/GaSb IMF and GaSb/GaSb control diodes. Region 1 is indicative of high series resistance, and region 2 is indicative of low shunt resistance.

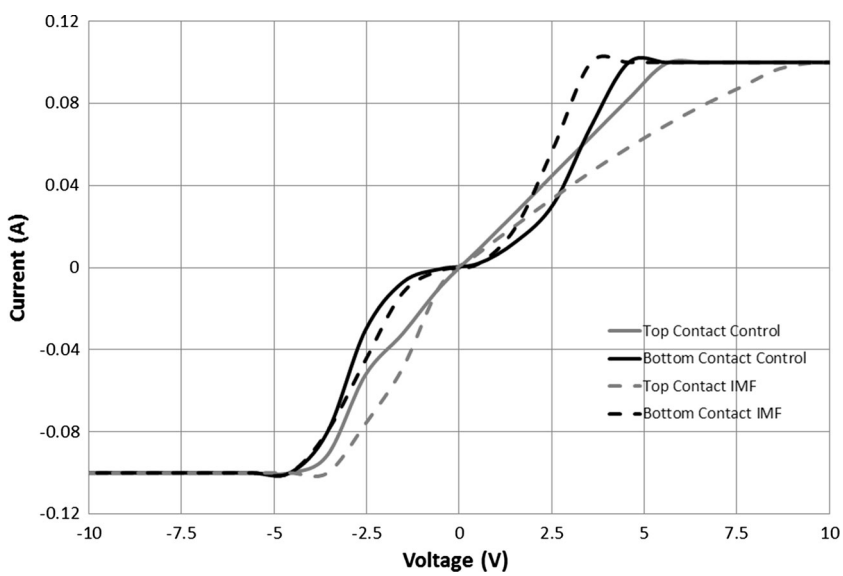


Fig. 5. *I–V* curves for the top and bottom contacts of the Ti-Pt-Au ohmic contact recipe on IMF sample.

likely caused by a high contact resistance, as evident from our contact measurements shown in Fig. 5. However, low shunt resistance is typically caused by manufacturing defects, which provide an alternate, low-resistance path for light-generated current. This phenomenon is indicated in the *I–V* curve by a negative slope on the top line between the short-circuit current and maximum-power point (region 2 of Fig. 4), and characteristically lowers the open-circuit voltage. We expect the decreased shunt resistance to be due to an increase in threading dislocations, which act as a short in the lower layers of the device. The open-circuit voltage is also affected by a potential barrier that must be overcome by the charge carriers, such as a Schottky diode, which will be investigated further.

While the inverse slope of the curve at $V_{OC}$ and $J_{SC}$ are often used as $R_{series}$ and $R_{shunt}$, respectively, this is an approximation that holds for well-behaved curves. The shape of the curve is a function of the ratio between $R_{shunt}$ and $R_{series}$ and tells nothing about the values themselves. Therefore, we decided to look into causes which lead to these parasitic

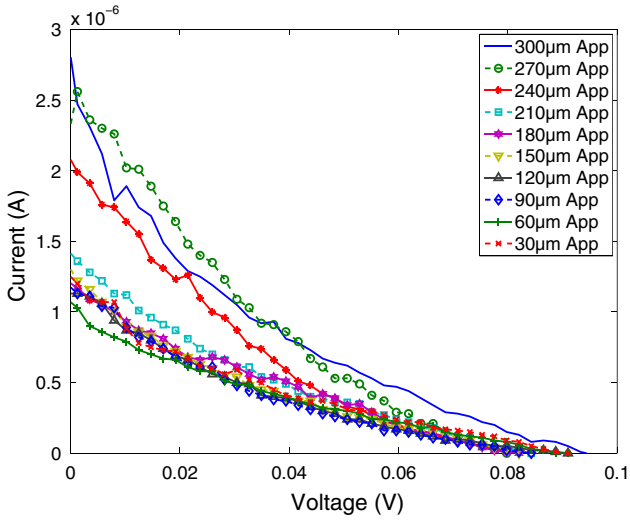


Fig. 6. *I–V* curves for the set of 10 aperture diodes. Lower current with smaller apertures is demonstrated as expected. The concave-down nature of the curve is not expected and is indicative of defects and Schottky contacts.

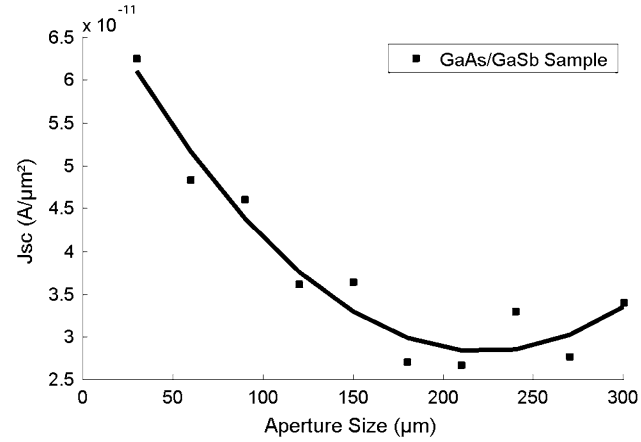


Fig. 7. Short-circuit current density versus aperture size. The black line is a fourth-order polynomial trend line. Decrease in $J_{SC}$ is due to surface defects and increased carrier travel distance.

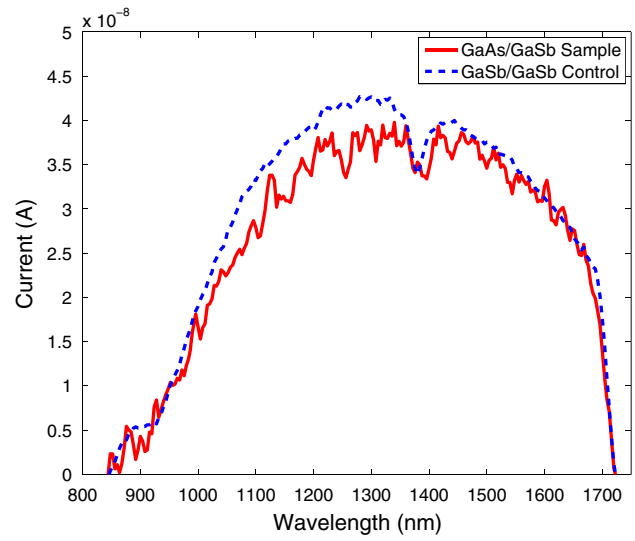


Fig. 8. Spectral response of GaAs/GaSb IMF sample and control. A moving average was applied to the data to reduce some of the noise.

resistances, including ohmic contact tests and transmission electron microscopy (TEM).

Ohmic contact tests, shown in Fig. 5, were performed to determine if the contacts were contributing to the performance of the device. For both the control and IMF sample, the top contact appears ohmic, yet highly resistive; however, the bottom contact displays Schottky characteristics below ~3 V. These contact recipes have shown ohmic characteristics in literature,[25,26] however these results warrant further investigation of ohmic contact to $n$-type GaSb. The Schottky barrier contact is likely contributing to the low $V_{OC}$ values, however it would affect both the sample and control; as such, we do not believe this to be the major contributor to the low performance of the IMF TPV cells.

The aperture diode *I–V* curves shown in Fig. 6 display similar results to the diodes shown in Fig. 4. The *I–V* curves in these cases are concave-up, as opposed to the normal concave-down curve. This is most likely caused by a combination of a large defect density, small aperture area, and Schottky electrical contact. Lower current as the aperture size decreases is expected and is due to less area for light absorption. It should be noted that the measured currents for the diodes in Fig. 6 are two orders of magnitude lower than measured for the IMF diode in Fig. 4, whereas the ratio of the areas for 500 $\mu$m diameter and 300 $\mu$m diameter is 9/25. This can be attributed to the fact that the set of 10 different sized apertures were fabricated near the edge of the sample wafer, where diodes typically perform worse than those fabricated at the center.[27] The performance of the 500-$\mu$m-aperture diode will also be higher due to the top electrical contact cross pattern, which decreases the carrier travel distance, thus reducing recombination.

To characterize potential defects, the short-circuit current densities are plotted versus aperture size in Fig. 7. The black line is a fourth-order polynomial trend line, which visually highlights the overall slight decrease in short-circuit current density. This serves to show the dependence that the short-circuit current has on aperture size, indicating that there are most likely surface defects in the sample. Additionally, this could also be a function of the increased distance that carriers need to travel to reach the electrical contacts due to the increased spacing of the active area. There is still a probability of recombination in the semiconductor contact layers, so increased distance between the metal electrical contacts increases the chance of recombination, thus lowering the current out.

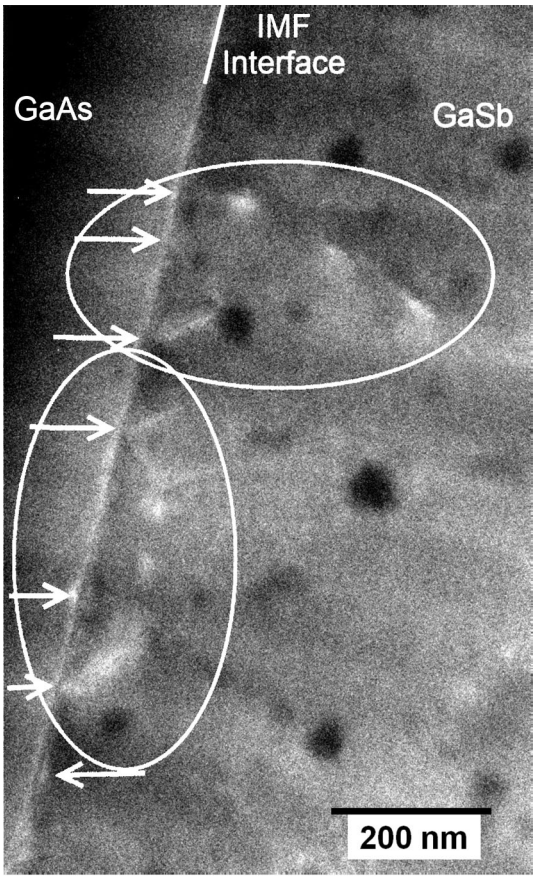


Fig. 9. TEM image of threading dislocations in the GaSb/GaAs IMF TPV sample. Origins of threading dislocations are marked by arrows, and the propagation of longer strands encircled with ellipses. Dark circles on the right are gallium agglomerations caused by the gallium ion beam interacting with the gallium in the sample.

The samples were also tested for spectral response, which is a relative measure of the current generated at each wavelength. As there has been little work with IMF absorbing materials, and no work on absorbers for the GaSb/GaAs material system, this absorbed spectral response is quite significant. The data are plotted in Fig. 8. The high noise is due in part to low optical transmission in the filtering grating of the monochromator; a moving average was applied to the data to smooth out the noise. Since the cutoff wavelength is just over 1700 nm, which corresponds to the bandgap of GaSb,[28] these data show that the absorption is occurring in the GaSb layers as expected. Two features of this graph indicate the superior performance of the control sample as compared with the IMF sample: the higher current output between 1000 nm and 1500 nm, and the decreased noise in the data over the entire curve. These characteristics indicate an increase in recombination in the IMF sample. This results in fewer carriers reaching the contacts, and an increased variability in the output due to the randomness of recombination processes.

A TEM image was taken of the GaAs/GaSb interface and can be seen in Fig. 9. The sample was prepared using focused ion beam milling. It shows the presence of threading dislocations propagating into the bottom contact layer of the IMF device. This is unexpected and shows that there were issues with the IMF array formation. This explains many of the results seen previously, such as poor bottom contact behavior, low shunt resistance, and poor diode performance.

## CONCLUSIONS

This work demonstrated GaSb thermophotovoltaic energy harvesters fabricated on highly lattice-mismatched GaAs substrates via the interfacial misfit array method. Photodiodes were fabricated and displayed a generated photocurrent. Through XRD analysis, it was concluded that initial IMF growths were sufficient in mitigating material strain; however, the formation of threading dislocations was sufficient to reduce device functionality. Reduced performance was not due to the underlying technique and methods, but due to unoptimized growth procedures for absorber devices. With further investigation into IMF absorber technologies, these issues are expected to be rectified. The next iteration of these devices will feature an improved diode design which is expected to further decrease the creation of threading dislocations.

## ACKNOWLEDGEMENTS

This material is based upon work supported by the National Science Foundation Graduate Research Fellowship under Grant No. DGE-0806676 and NSF Grant No. ECCS-1055203. This work was performed in part at the Center for Nanoscale Systems (CNS), a member of the National Nanotechnology Infrastructure Network (NNIN), which is supported by the National Science Foundation under NSF Award No. ECS-0335765. CNS is part of Harvard University. The Tufts Micro- and Nanofabrication Facility was also used for this work.

## REFERENCES

1. D.F. DeMeo and T.E. Vandervelde, *MRS Proc.* 1329 (2011).
2. C. Shemelya and T.E. Vandervelde, *J. Electron. Mater.* 41, 928 (2012).
3. C.M. Shemelya and T.E. Vandervelde, *MRS Proc.* 1208, 1208 (2011).
4. D.F. DeMeo and T.E. Vandervelde, *J. Vac. Sci. Technol. B Microelectron. Nanom. Struct.* 29, 031401 (2011).
5. D.L. Chubb, *Fundamentals of Thermophotovoltaic Energy Conversion* (Amsterdam: Elsevier, 2007), p. 515.
6. Y.B. Bolkhovityanov and O.P. Pchelyakov, *Phys. Usp.* 51, 437 (2008).
7. S.H. Huang, G. Balakrishnan, A. Khoshakhlagh, A. Jallipalli, L.R. Dawson, and D.L. Huffaker, *Appl. Phys. Lett.* 88, 131911 (2006).
8. A. Jallipalli, G. Balakrishnan, S.H.H. Huang, A. Khoshakhlagh, L.R.R. Dawson, and D.L.L. Huffaker, *J. Cryst. Growth* 303, 449 (2007).

9. M. Mehta, G. Balakrishnan, S. Huang, A. Khoshakhlagh, A. Jallipalli, P. Patel, M.N. Kutty, L.R. Dawson, and D.L. Huffaker, *Appl. Phys. Lett.* 89, 211110 (2006).
10. S. Huang, G. Balakrishnan, and D.L. Huffaker, *J. Appl. Phys.* 105, 103104 (2009).
11. C. Downs and T.E. Vandervelde, *Sensors (Basel)* 13, 5054 (2013).
12. T.E. Vandervelde and S. Krishna, *J. Nanosci. Nanotechnol.* 10, 1450 (2010).
13. A. Barve, J. Shao, Y.D. Sharma, T.E. Vandervelde, K. Sankalp, S.J. Lee, S.K. Noh, and S. Krishna, *IEEE J. Quantum Electron.* 46, 1105 (2010).
14. J.R. Andrews, S.R. Restaino, S.W. Teare, Y.D. Sharma, W.-Y. Jang, T.E. Vandervelde, J.S. Brown, A. Reisinger, M. Sundaram, S. Krishna, and L. Lester, *IEEE Trans. Electron Devices* 58, 2022 (2011).
15. R.V. Shenoi, J. Rosenberg, T.E. Vandervelde, O.J. Painte, and S. Krishna, *IEEE J. Quantum Electron.* 46, 1051 (2010).
16. J. Rosenberg, R.V. Shenoi, T.E. Vandervelde, S. Krishna, and O. Painter, *Appl. Phys. Lett.* 95, 161101 (2009).
17. J. Shao, T.E. Vandervelde, W.-Y. Jang, A. Stintz, and S. Krishna, *2008 8th IEEE Conference on Nanotechnology (IEEE, 2008)*, pp. 112–115.
18. P. Vines, C.H. Tan, J.P.R. David, R.S. Attaluri, T.E. Vandervelde, S. Krishna, W.-Y. Jang, and M.M. Hayat, *IEEE J. Quantum Electron.* 47, 190 (2011).
19. P. Vines, C.H. Tan, J.P.R. David, R.S. Attaluri, T.E. Vandervelde, and S. Krishna, *SPIE Eur. Secur. Def.*, ed D.A. Huckridge and R.R. Ebert (Bellingham, WA: International Society for Optics and Photonics, 2008), pp. 71130J–71130J-7.
20. S. Adachi, P. Capper, and S. Kasap, *Properties of Semiconductor Alloys: Group-IV, III–V and II–VI Semiconductors* (New York: Wiley, 2009).
21. S. Huang, G. Balakrishnan, and D. Huffaker, *Microsc. Microanal.* 15, 1062 (2009).
22. A. Jallipalli, G. Balakrishnan, S. Huang, T. Rotter, K. Nunna, B. Liang, L. Dawson, and D. Huffaker, *Nanoscale Res. Lett.* 4, 1458 (2009).
23. C.J. Reyner, J. Wang, K. Nunna, A. Lin, B. Liang, M.S. Goorsky, and D.L. Huffaker, *Appl. Phys. Lett.* 99, 231906 (2011).
24. K.C. Nunna, S.L. Tan, C.J. Reyner, A.R.J. Marshall, B. Liang, A. Jallipalli, J.P.R. David, and D.L. Huffaker, *IEEE Photonics Technol. Lett.* 24, 218 (2012).
25. A. Jallipalli, M.N. Kutty, G. Balakrishnan, J. Tatebayashi, N. Nuntawong, S.H. Huang, L.R. Dawson, D.L. Huffaker, Z. Mi, and P. Bhattacharya, *Electron. Lett.* 43, 1198 (2007).
26. F.Y. Soldatenkov, S.V. Sorokina, N.K. Timoshina, V.P. Khvostikov, Y.M. Zadiranov, M.G. Rastegaeva, and A.A. Usikova, *Semiconductors* 45, 1219 (2011).
27. W.C. Riordan, R. Miller, J.M. Sherman, and J. Hicks, *1999 IEEE International Reliability Physics Symposium Proceedings. 37th Annual. (Cat. No. 99CH36296) (IEEE, 1999)*, pp. 1–11.
28. P.S. Dutta, H.L. Bhat, and V. Kumar, *J. Appl. Phys.* 81, 5821 (1997).